



HAL
open science

In-Cylinder Thermographic PIV Combined with Phosphor Thermometry using ZnO:Zn

Andreas Kopf, Valerio Frattina, Michele Bardi, Torsten Endres, Gilles
Bruneaux, Christof Schulz

► **To cite this version:**

Andreas Kopf, Valerio Frattina, Michele Bardi, Torsten Endres, Gilles Bruneaux, et al.. In-Cylinder Thermographic PIV Combined with Phosphor Thermometry using ZnO:Zn. *International Journal of Engine Research*, 2023, 24 (1), pp.113-131. 10.1177/14680874211048559 . hal-03945496

HAL Id: hal-03945496

<https://ifp.hal.science/hal-03945496>

Submitted on 18 Jan 2023

HAL is a multi-disciplinary open access archive for the deposit and dissemination of scientific research documents, whether they are published or not. The documents may come from teaching and research institutions in France or abroad, or from public or private research centers.

L'archive ouverte pluridisciplinaire **HAL**, est destinée au dépôt et à la diffusion de documents scientifiques de niveau recherche, publiés ou non, émanant des établissements d'enseignement et de recherche français ou étrangers, des laboratoires publics ou privés.

1 In-cylinder thermographic PIV combined with phosphor 2 thermometry using ZnO:Zn

3 **A. Kopf^{a,b,*}, V. Frattina^{a,b}, M. Bardi^a, T. Endres^b, G. Bruneaux^a, C. Schulz^b**

4
5 ^aIFP Energies Nouvelles, 1 et 4 Avenue de Bois-Préau, 92852 Rueil-Malmaison Cedex, France; Institut Carnot IFPEN
6 Transports Energie

7 ^bIVG, Institute for Combustion and Gas Dynamics – Reactive Fluids, and CENIDE, Center for Nanointegration, University of
8 Duisburg-Essen, Germany

9
10 **E-Mail address:** andreas.kopf@posteo.net

11 **Abstract**

12 Two-dimensional thermographic particle image velocimetry (T-PIV) is presented for the *in situ*
13 measurement in optically accessible internal combustion (IC) engines. Temperature and velocity
14 measurements are combined using thermographic phosphor particles as tracers for PIV. For three
15 commercially available phosphors (BAM:Eu²⁺, ZnO, and ZnO:Zn), temperature sensitivity, luminescence
16 intensity at high temperatures and laser-fluence dependences were evaluated for phosphor-coated surfaces
17 in a high-temperature cell. ZnO:Zn was identified as the best-suited candidate for engine in-cylinder
18 measurements and further analyzed in the aerosolized state at temperatures up to 775 K to generate
19 calibration data required for signal quantification in engine experiments. T-PIV was successfully applied
20 in the IC engine to simultaneously obtain instantaneous two-dimensional velocity and temperature fields
21 using the intensity-ratio method. Despite a measurement uncertainty ($\pm 1\sigma$ basis) of only 3.7 K at 317 K
22 (1.2 %) to 24.4 K (4.2 %) at 575 K, this technique suffers from low signal intensities due to thermal
23 quenching at increasing temperatures, which leads to reduced accuracy as the piston approaches top dead
24 center (TDC). Thermographic measurements were successful to visualize local temperature changes due
25 to evaporative cooling after fuel injection. The measured mean gas temperatures agreed well with zero-
26 dimensional simulations that use additional wall-temperature measurements from thermographic phosphor
27 measurements based on the lifetime method as input for heat transfer calculations.

28
29 **Keywords:** thermographic phosphors, thermographic PIV, *in situ* thermometry, internal combustion
30 engine, ZnO:Zn.

31

1 Abbreviations and acronyms

2

AMESim	Advanced modeling environment for performing simulations of engineering systems
ASI	After start of injection
ε	Geometric compression ratio
CA	Crank angle
CAD	Crank angle degree
CCD	Charge-coupled device
FWHM	Full width at half maximum
HCCI	Homogeneous-charge compression ignition
ICE	Internal combustion engine
LIF	Laser-induced fluorescence
PIV	Particle image velocimetry
PMT	Photomultiplier tube
RPM	Revolutions per minute
TDC	Top dead center
TR	Tumble ratio
TP	Thermographic phosphor
Y_f	Fuel mass fraction

3

4

5

2 Introduction

The knowledge of fluid temperature and velocity is crucial in many practical combustion processes to design and improve these processes. For reciprocating internal combustion engines (ICEs), both parameters play an important role for almost all processes throughout an engine cycle, such as fuel evaporation, mixing, chemical kinetics, wall heat transfer, and pollutant formation [1–5]. For velocity measurements in fluid flows, particle image velocimetry (PIV) is a well-established technique using particles as tracers for observing the fluid motion in a two-step imaging process. *In situ* gas-phase temperature imaging measurements in reacting flows are often achieved by Rayleigh scattering [6] or laser-induced fluorescence using organic tracers [7] or naturally-occurring species (e.g., OH, NO [8,9]). These methods can be combined with PIV to derive information about the fluid flow and the temperature simultaneously, e.g., via tracer-LIF [10] or filtered Rayleigh scattering [11]. However, the latter is related to a considerable experimental effort and complexity as the presence of particles used for PIV interferes with the elastically scattered laser light for Rayleigh measurements.

Temperature measurements using thermographic phosphors are frequently performed for surface measurements, but recently this technique has been extended to gas-phase temperature measurements [12]. It is of interest to combine temperature and velocity measurements using thermographic phosphors to simplify experimental complexity and to share equipment. Thermographic particle image velocimetry (T-PIV) enables the simultaneous imaging measurement of temperature and flow velocity in challenging conditions as those found in ICEs. In T-PIV, thermographic phosphor (TP) particles are seeded into the flow and are exploited for two diagnostics methods. Firstly, the particles can be used as tracers for velocity measurements following the conventional double-pulse PIV approach. But secondly, the luminescence from the same particles is employed to measure the local temperature of the fluid.

Thermographic phosphors feature temperature-dependent luminescence upon laser excitation and the emitted luminescence can therefore be used for temperature sensing. This method is of particular interest for the application in reacting flows, since most of TPs are chemically inert and insensitive to pressure [13]. While the luminescence properties of BAM:Eu²⁺ (referred to here as BAM:Eu) was found to be insensitive to oxygen for gas compositions up to 200 mbar partial pressure [14], no systematic investigations of the influence of oxygen on ZnO are available in literature so far, annealing conditions to change the luminescence properties of ZnO are usually on the order of hours in oxygen atmosphere at high temperatures (up to 1050 °C) [15], thus luminescence properties are not expected to be affected from short residence times and moderate temperatures as found during compression and expansion in the engine . .

While the feasibility of this combined technique has been demonstrated in turbulent gas flows [17], the application in internal combustion engines faces various challenges such as fast fluid motion, seeding

1 fluctuations due to inherent cyclic variations in the intake manifold, and low signal intensities. For fired
2 operation, the signal can also interfere with flame luminescence and particles can deteriorate once exposed
3 to the flame [16]. Therefore, TPs with short radiative lifetimes as well as strong signal yield at high
4 temperatures are preferred. It is equally important to select a phosphor with a high temperature sensitivity
5 to obtain good measurement precision in the temperature range of interest.

6 Phosphor thermometry was carried out before in an engine environment using phosphors with long
7 luminescence lifetimes for time-averaged surface temperature measurements on a piston crown using
8 $\text{La}_2\text{O}_2\text{S:Eu}$ [18] or on a transparent cylinder wall [19,20]. Hasegawa et al. [21] performed gas-phase TP
9 measurements before and during HCCI combustion and they were able to identify flame kernels from
10 temperature measurements using YAG:Dy, but interference from combustion luminescence emission
11 prevented measurements later than 350 CAD due to long luminescence lifetimes ($\sim 100 \mu\text{s}$) [21,22].
12 Aerosol temperature measurements were conducted in a Diesel piston bowl with YAG:Dy³⁺ and BAM:Eu,
13 where the latter was used when the piston approaches TDC due to stronger emission intensities. However,
14 the temperature sensitivity of BAM:Eu is usually in the range of 0.2 %/K, and thus the limiting factor for a
15 high measurement precision. Furthermore, measurements using thermographic phosphors were only
16 possible up to 3 CAD after start of injection (ASI) due to strong signal contribution from
17 chemiluminescence [23]. Combined T-PIV measurements in an optical engine were performed for the first
18 time by Neal et al. using YAG:Pr at three different crank angle positions in the compression stroke,
19 achieving a single-shot precision (1σ) as good as 20 K at 600 K [24]. Due to phosphor excitation at
20 266 nm using YAG:Pr, the authors found systematic interference from the window material.

21

22 **2.1 Measurement strategy**

23 With thermographic phosphors, temperature can be measured by either exploiting the temperature-
24 dependence of the luminescence lifetime, the shape of the emission spectra, or the signal intensity. The
25 lifetime method evaluates the signal decay in the time domain. The temperature-dependent variation in
26 emission spectra is often recorded based on the intensity ratio from two spectrally separated wavelength
27 ranges selected by filters. For 2D imaging measurements, the first requires a single camera with a frame
28 rate fast enough to capture the signal decay after laser excitation in multiple frames, the latter requires two
29 cameras with single exposure per laser pulse. For both approaches, the temperature is then inferred from a
30 calibration curve, where the lifetime or the intensity ratio has been measured for a respective temperature
31 range in a controlled environment. The intensity-based method requires a reference such as temperature-
32 independent elastic scattering (Mie signal) and therefore, also two separate detectors [29].

1 For all strategies, it is crucial to know the related temperature-dependent signal changes from reliable
2 calibration measurements. Several previous studies revealed that the luminescence properties of
3 thermographic phosphors vary according to its agglomeration state (bulk powder, surface coating, liquid
4 dispersion, or aerosol). Jovicic et al. observed different optical properties for YAG:Dy and YAG:Er,Dy
5 when varying the agglomeration state. They found an error of 9.4 % in determining the temperature at
6 447 K that is caused by applying calibration data from coatings to aerosol measurements [25]. Fond et al.
7 investigated various phosphors (BAM:Eu, Mg₄FGeO₆:Mn, (Sr, Mg)₃(PO₄)₂:Sn, ZnO) and showed that the
8 emission properties vary significantly between bulk powder and liquid dispersion [26]. For ZnO they
9 found a signal per unit mass that was 500 times stronger in liquid dispersion compared to powder. For
10 BAM:Eu, Witkowski and Rothamer [27] observed red-shifted emission in powder measurements
11 compared to aerosol measurements attributed to radiative trapping in the powder. This leads to an
12 underestimation of temperature, larger than 100 K at 700 K for measurements in environments with high
13 phosphor concentrations such as bulk powder in a furnace. Hertle et al. characterized (Sr,Ca)SiAlN₃:Eu²⁺
14 in bulk powder and surface coatings between ambient temperature and 773 and 548 K respectively. The
15 spectral emission from the surface coatings at room temperature showed a significant blue-shift compared
16 to the bulk powder measurements that was attributed to radiative trapping in the powder and to decreased
17 crystal field strength in the coated phosphor due to the presence of the binder [28]. These studies strongly
18 suggest that the agglomeration state of a phosphor should be consistent throughout the calibration and the
19 measurements in the system of interest.

20 One of the main objectives of this study is to test various phosphors (BAM:Eu, ZnO and ZnO:Zn) with
21 short radiative lifetimes, high temperature sensitivity, and strong signal levels at elevated temperatures
22 with the aim of improving measurement reliability at high temperature and under fast transient conditions
23 in an optical engine. BAM:Eu and ZnO have been frequently applied for temperature measurements, but
24 only limited information about the properties of ZnO:Zn is available in literature. In this work, a
25 preliminary screening from measurements on coated surfaces was carried out to compare three
26 commercially available phosphors with limited experimental effort, followed by a comprehensive aerosol
27 characterization for the most promising phosphor. In screening measurements, ZnO:Zn showed promising
28 properties such as high quenching temperature and low non-linear dependence on laser fluence, and the
29 highest temperature sensitivity of all three phosphors for the temperature range of interest in the engine
30 (400–700 K). Therefore, the aerosol characterization focused on ZnO:Zn, investigating the influence of
31 the seeding density and the laser fluence on the luminescence properties. Spectrally-resolved calibration
32 data was acquired from aerosols heated in a tube furnace covering the temperature range from 300 to
33 775 K. A ratio-based temperature calibration curve is obtained from the spectral calibration data using the
34 transmission characteristics of the bandpass filters used in the engine measurements. T-PIV imaging is

1 then carried out in an optically-accessible engine under motored conditions with and without fuel injection
2 using ZnO:Zn. To the authors' knowledge, these are the first in-cylinder thermographic phosphor
3 measurements employing aerosol-based calibration.

4 This paper is organized as follows. In section 3.1, the properties of three commercial phosphors (BAM:Eu,
5 ZnO and ZnO:Zn) are described based on measurements on coated surfaces in a high-temperature cell to
6 evaluate the most suitable phosphor for engine measurements. ZnO:Zn was chosen based on its properties
7 in terms of thermal quenching, temperature sensitivity, and laser fluence dependence. The arrangement for
8 aerosol calibration and engine measurements are shown in section 3.3 and 3.4, respectively. The
9 procedure for data post-processing is shown in section 3.5. The section 3.6 describes zero-dimensional
10 simulations of the engine process using additional wall-temperature measurements as input for the heat
11 transfer calculation. In section 4, the results are presented and compared to the simulation results and error
12 sources are analyzed.

13 **3 Materials and methods**

14 **3.1 Phosphor selection**

15 For applications in engines combining two-color phosphor thermometry and PIV, the following optical
16 requirements must be met: Small particle diameters to quickly follow changes in temperature and velocity,
17 high temperature sensitivity in the range of 400–700 K to provide good measurement precision, short
18 radiative lifetimes and strong signal intensities at increased temperatures and to discriminate against signal
19 interference from combustion or blackbody radiation, and resistance to combustion for post-flame
20 measurements. Furthermore, there are hardware limitations using an optical engine: High hardness of the
21 phosphor will accelerate wear of engine parts such as the optical cylinder or piston rings. This effect has
22 not been analyzed quantitatively, but significant differences were found for the phosphor materials.
23 Phosphor excitation at 355 nm is preferred over 266 nm to reduce interference from fluorescence from
24 fuel components, intermediate combustion species, or optical elements. Additionally, a measurement
25 campaign requires several 100 grams of phosphor material, which favors the use of off-the-shelf materials.
26 Three commercially available phosphors (BAM:Eu, ZnO, ZnO:Zn, provided by Phosphor Technology
27 KEMK63, Sigma Aldrich 96479, Phosphor Technology GK30, respectively), all excitable at 355 nm,
28 were evaluated first based on measurements on a coated surfaces in a high-temperature cell considering
29 the applicable temperature range, temperature sensitivity or non-linear dependence of phosphor emission
30 to laser fluence. BAM:Eu and ZnO are well characterized and one of the most frequently applied
31 phosphors for fluid measurements [26,30], therefore the focus was placed on ZnO:Zn.

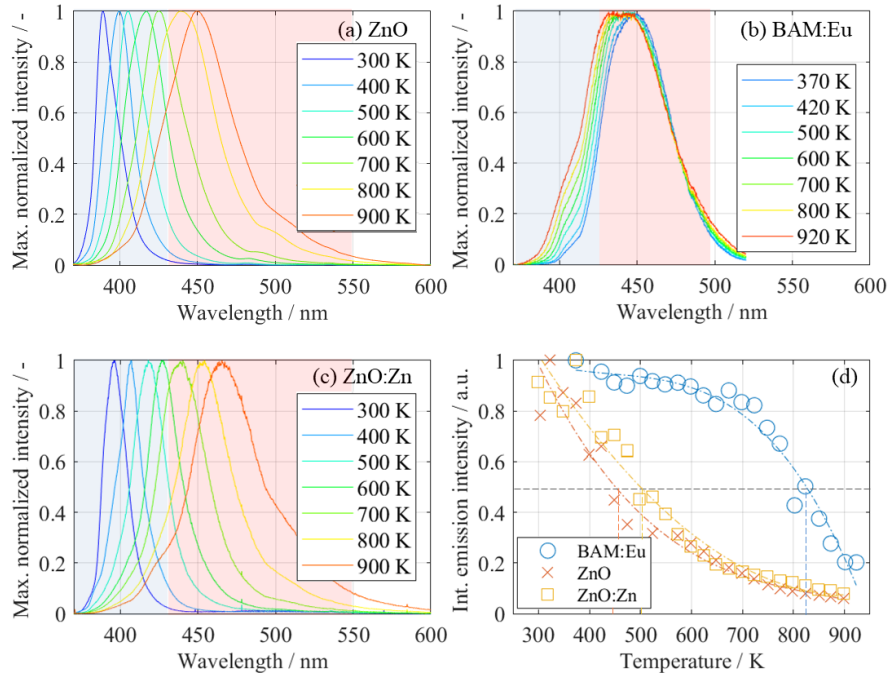
1 ZnO is a direct semiconductor with a band gap of 3.37 eV and exciton binding energy of 59 meV at
2 ambient temperature [15,31]. Upon laser excitation, ZnO exhibits a near-band-edge emission from the
3 exciton states, centered at ~380 nm with an emission lifetime of less than 1 ns [19]. ZnO shows broadband
4 emission centered at 510 nm with an emission decay ($1/e$) of ~1 μ s at room temperature, which is three
5 orders of magnitude longer than the one of the near-UV emission [32]. The green emission has been
6 attributed to ZnO annealing in low-oxygen atmosphere leading to oxygen vacancies that result in Zn-
7 enriched zinc oxide (ZnO:Zn) with 510-nm (2.43 eV) intraband emission [15]. Both emissions can be
8 exploited for temperature measurements: The UV emission shows a pronounced redshift that can be used
9 for high-sensitivity intensity-ratio temperature measurements, whereas the temperature dependence of the
10 green emission enables temperature sensing in the time domain showing a change in luminescence
11 lifetime of a factor larger than 30 between room temperature and 460 K [32]. When performing intensity-
12 ratio measurements, the green emission can interfere with the spectral acquisition band used for intensity-
13 ratio measurements, however it can be efficiently suppressed using a gated camera. In literature, the
14 intensity-ratio method was applied using ZnO:Zn to monitor the temperature distribution on a burner plate
15 with a sensitivity superior to 60 mK [33]. ZnO:Ga was used for 2D temperature measurements in a
16 burning methanol droplet [34]. The combination of a short radiative lifetime (<1 ns) and strong sensitivity
17 to temperature changes makes this phosphor an excellent candidate for temperature measurements in
18 challenging environments such as IC engines.

19 **3.2 Phosphor screening on surface measurements**

20 The phosphor particles were coated on a metal surface (HPC binder, ZYP coating) and heated to 920 K in
21 a high-temperature cell. The phosphors were excited with the radiation from a frequency-tripled Nd:YAG
22 laser (355 nm, SpectraPhysics, INDI-50) with beam homogenizer with a fluence of 10 mJ/cm². The
23 luminescence was collected with a spherical lens ($f = 300$ mm), spectrally dispersed (Acton SP-300,
24 grating 300 g/mm, 300 μ m entrance slit) and detected with an ICCD camera (PIMAX, Princeton
25 Instruments). The spectral resolution was 1 nm (full-width at half maximum) as determined with a
26 mercury lamp and the wavelength-dependent sensitivity of the detection system was calibrated against a
27 tungsten halogen lamp.

28

29

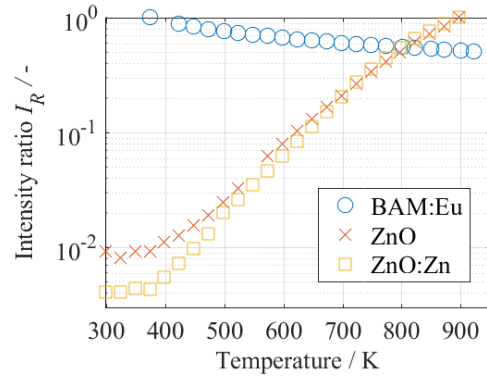


1
 2 Figure 1: Normalized emission spectra from coated surface experiments for ZnO, BAM:Eu, and ZnO:Zn (a–c). The band-integrated
 3 emission intensity for all three phosphors is shown in (d), where the quenching temperatures T_{50} are pointed out with a dashed line.
 4 The spectral regions highlighted in red and blue (a–c) show the ideal filter transmission bands used for intensity ratio and temperature
 5 sensitivity calculations, see text.

6 Figure 1a–c shows the temperature-dependent emission spectra for ZnO, BAM:Eu, and ZnO:Zn. The
 7 spectra are normalized towards maximum intensity for each temperature. Figure 1d represents the
 8 integrated emission over the entire spectral range shown in the figure (370 to 520 nm for BAM:Eu and
 9 370 to 600 nm for both ZnO phosphors) to evaluate the influence of thermal quenching. The quenching
 10 temperature T_{50} , where the band-integrated luminescence drops to 50 % of its value at room temperature is
 11 an important measure to estimate signal yields at increasing temperatures. The quenching temperatures for
 12 BAM:Eu, ZnO, and ZnO:Zn were 825, 448, and 500 K, respectively. If the measurement of ZnO at
 13 ambient temperature (300 K) is considered an outlier, T_{50} for ZnO would be even lower.

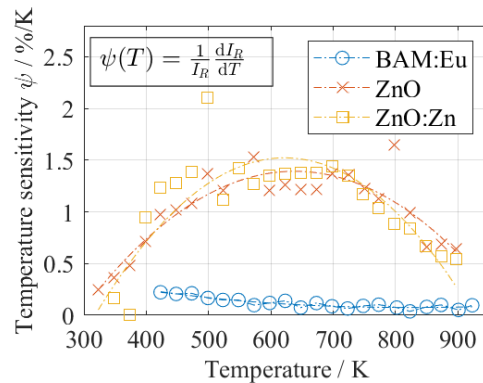
14 Non-linear signal response on laser fluence can lead to a bias in temperature determination if it is not
 15 accounted for. Linear signal increase from 0.45–2 mJ/cm² with the excitation fluence was found for
 16 BAM:Eu, followed by non-linear signal response up to 10 mJ/cm². This is qualitatively in agreement with
 17 literature data for aerosolized BAM:Eu [14,35]. Similarly to BAM:Eu, a non-linear signal response was
 18 found for ZnO from 5 to 10 mJ/cm², which was previously described in Ref. [36]. On the contrary, the
 19 luminescence intensity of ZnO:Zn increased linearly up to 10 mJ/cm², which decreases the bias in
 20 temperature calculation for varying fluences.

1 For thermometry applications, finding phosphors with a high temperature sensitivity is equally important
 2 as to overcome the limitation from low signal intensity at high temperatures. The shift in the spectrum of
 3 BAM:Eu is less distinct than for both ZnO phosphors, leading to a relatively lower temperature sensitivity.
 4 While the emission of both ZnO-based phosphors is qualitatively similar, ZnO:Zn features a more
 5 pronounced red-shift than ZnO, making it more sensitive to temperature variations. Figure 2 shows the
 6 intensity ratio and the calculated temperature sensitivity ψ assuming idealized bandpass filters with a top-
 7 hat transmission characteristic (blue: 370–430 nm, red: 430–550 nm for both ZnO phosphors and blue:
 8 370–430 nm, red: 430–500 nm for BAM:Eu, cf. color-shaded areas in Figure 1). These filter
 9 characteristics for BAM:Eu are similar to the filter combinations suggested in Ref. [14] and the filters for
 10 both ZnO-phosphors are identical to enable direct comparison. In the range between 400 and 700 K,
 11 ZnO:Zn has an average temperature sensitivity of around 1.42 %/K, which is slightly higher than ZnO
 12 (1.29 %/K) and more than ten times higher than the temperature sensitivity for BAM:Eu (0.13 %/K).



13

14



15

16 Figure 2: Intensity ratio (top) and normalized temperature sensitivity ψ (bottom) for the investigated phosphors. The intensity
 17 ratio was calculated by dividing the band-integrated emission intensity determined by the filters. Idealized filter transmission
 18 characteristics are assumed for all phosphors, see text. The temperature sensitivity was calculated from the intensity ratio
 19 according to the formula shown in the top left corner.

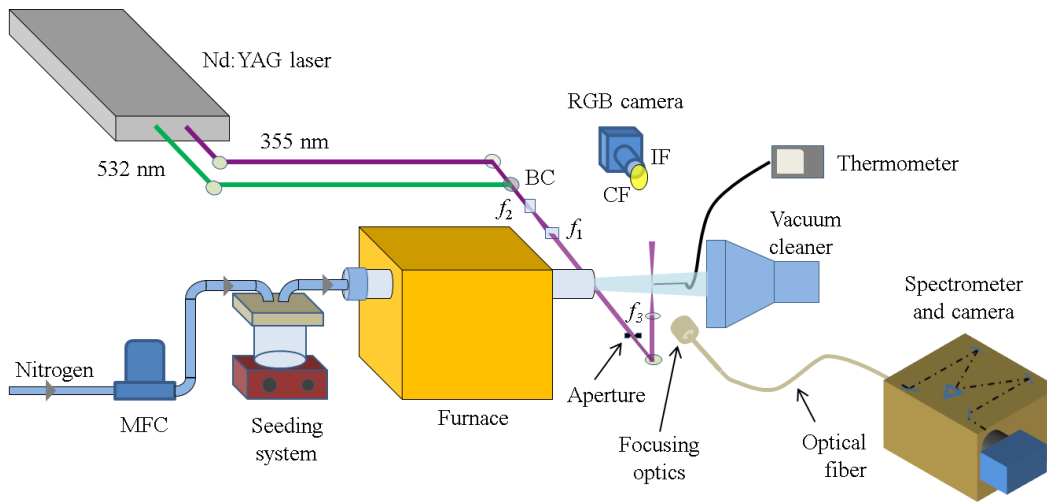
1 The characterization of the phosphors' luminescence properties from coated-surface experiments shows
2 that the quenching temperature of BAM:Eu is higher than for the two ZnO-based phosphors, but
3 significantly lower in sensitivity to a change in temperature. However, ZnO has higher per-particle
4 luminescence emission than BAM:Eu, but ZnO shows stronger non-linear dependence on laser fluence
5 [26,30]. The higher temperature sensitivity and the more elevated quenching temperature T_{50} of ZnO:Zn
6 relatively to ZnO, and particularly the absence of saturation effects in the investigated range of fluences
7 make ZnO:Zn the most attractive phosphor for highly sensitive thermographic measurements in the
8 temperature range relevant for in-cylinder measurements.

9 **3.3 Phosphor characterization in the aerosol phase**

10 A high-temperature furnace with controlled heating up to 775 K was used for heating an aerosol flow of
11 ZnO:Zn ($d_{50} = 3.5 \mu\text{m}$) in a 17-mm diameter quartz tube. A 1.5-mm diameter K-type thermocouple was
12 used to measure the gas temperature at the furnace outlet in the proximity of the probe volume of the
13 optical detection system. The particles were dispersed in the air using an in-house seeder equipped with a
14 magnetic stirrer and flown through the tube with an exit velocity between ~ 23 and 46 cm/s. The seeding
15 density was controlled by adapting the nitrogen mass flow rate through the seeder at constant seeding
16 operation. Prior to the measurements, phosphor particles were dried at 150 °C for four hours to decrease
17 particle agglomeration. The aerosol homogeneity was improved by adding nanometer-sized SiO₂ particles
18 that prevent agglomeration of phosphor particles, following the procedure of similar works [37–39]

19 A dual-cavity Nd:YAG laser (BMI Double Channel Series 5000, PVL 400) illuminated the test section
20 through two beams of different wavelengths: The frequency-tripled 355-nm output was used for phosphor
21 excitation, while the frequency-doubled output at 532 nm was used to measure the particle number density
22 via Mie scattering. Both beams are overlapped by a dichroic beam combiner (BC) and formed into a laser
23 sheet (800 μm thick and 20 mm high) using two cylindrical lenses ($f_1 = -150 \text{ mm}$, $f_2 = 200 \text{ mm}$) and a
24 spherical lens ($f_3 = 60 \text{ mm}$). The fluence of the 355 nm beam in the probe volume was 20–90 mJ/cm². The
25 phosphor emission was collected by an optical fiber with focusing optics, spectrally dispersed by a
26 spectrometer (Horiba iHR 320, $f = 320 \text{ mm}$, 300 lines/mm grating, 1-mm slit width) and detected by an
27 interline-transfer CCD camera (UV-VIS Syncerity) with an exposure time of 1 μs . The spectral sensitivity
28 of the detection system was detected against a calibrated tungsten halogen lamp integrated in an Ulbricht
29 sphere. A consumer camera (Nikon D5100, 2464 \times 1632 pixels, 16 \times 16 μm^2 pixel size) equipped with a
30 Nikkor lens ($f = 105 \text{ mm}$, $f/2.8$) and a transmission interference filter (IF, 532 \pm 4 nm, ML1 Microcoatings
31 Inc.) was used for detecting the number density of individual particles via elastic scattering of the 532-nm
32 laser beam. A color glass filter (CF, Schott OG515) was necessary to suppress signal contribution from

1 phosphorescence and scattering of the 355 nm laser light, despite the strong light rejection of the
2 interference filter.



3
4 Figure 3: Experimental layout for the spectral characterization of aerosolized ZnO:Zn and particle counting system.

6 3.4 Optical engine experiments

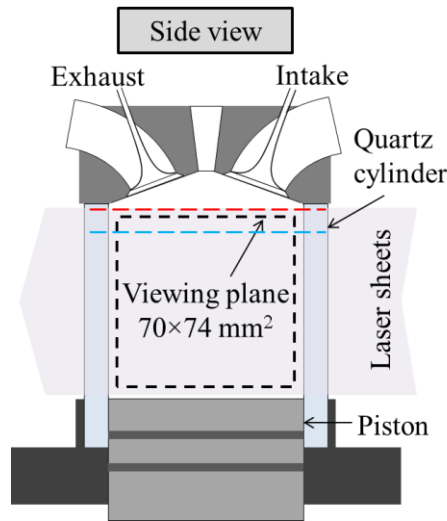
7 For in-cylinder measurements in an optically accessible engine, ZnO:Zn particles were dispersed in the air
8 fed into the engine intake manifold and used to measure temperature through two-color phosphor
9 thermometry and fluid flow velocity via PIV.

10 A single-cylinder, four-valve double over-head camshaft (DOHC) optical research engine with a fully
11 transparent cylinder (fused silica, corning 7980) is used for simultaneous temperature and velocity
12 measurements. The displacement volume of the engine is 399.5 cm^3 with a bore and stroke of 77 and
13 85.8 mm, respectively, and a geometric compression ratio $\varepsilon = 10.5$. The engine is equipped with a flat
14 piston crown in Bowditch layout [40] and a pent-roof cylinder head. The direct injection, spark-ignition
15 (DISI) engine is designed and manufactured by IFPEN [41] and features a five-hole centrally mounted
16 injector (Bosch HDEV 5.2).

17 A standard test case and two parametric variations (intake temperature, tumble) are investigated in this
18 work under motored conditions. The nominal engine speed is 1200 RPM and the injection system is
19 operated at 200 bar. The intake manifold temperature for the reference condition is 298 K with a tumble
20 ratio of $TR = 1.1$. The tumble is characterized on an in-house flow bench according to the methodology in
21 [40]. The calculation of the tumble ratio is detailed in the appendix A1. In the second test case, the intake
22 temperature is increased to 333 K. For the third operating condition, the engine is operated with standard

1 intake temperature (298 K) and the tumble ratio is increased by 15 % ($TR = 1.25$) using tumble flaps. For
2 all three test cases the temperature and velocity field are calculated during the compression and expansion
3 stroke over a wide range of crank angle degrees.

4

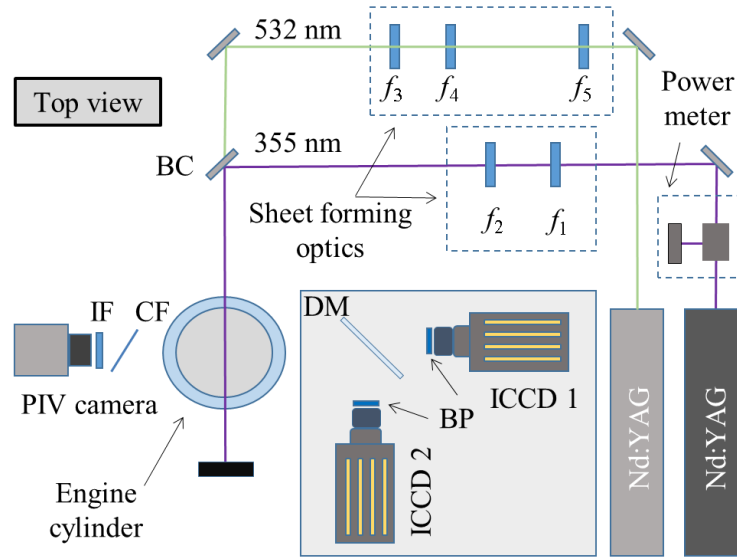


5

6 Figure 4: Side view of the optical engine used for T-PIV. The red dashed line shows the visualization limits due to the layout of
7 the engine cylinder head. The blue line shows the piston position at 330 and 390 CAD, resulting in a field of view of approx.
8 $70 \times 9 \text{ mm}^2$.

9 Due to the engine layout, visualization around top-dead center is not possible after 330 and before
10 390 CAD due to blockage of the optical cylinder by the piston. The 355-nm (SpectraPhysics, Quanta-Ray
11 GCR-150, 20 mJ/pulse, laser fluence: 50 mJ/cm^2) and 532-nm (Quantronix, Hawk-Duo, 5 mJ/pulse) laser
12 sheets are combined using a dichroic mirror and penetrate the optical cylinder vertically, resulting in an
13 illuminated area of $70 \times 74 \text{ mm}^2$. The cylindrical shape of the optical cylinder further focuses the light
14 sheets, leading to ~ 0.5 -mm thick light sheets inside the optical cylinder. Both lasers are operated at 10 Hz
15 and synchronized with the engine through a crank-angle encoder.

1



2

3 Figure 5: Optical layout used for in-cylinder temperature and velocity measurements. $f_1 = 1000$ mm, $f_2 = f_3 = -100$ mm,
4 $f_4 = 1100$ mm, $f_5 = 2000$ mm.

5 The signals were detected at right angles through the transparent cylinder wall (Figure 5). The distortion
6 of the collected images resulting from the cylindrical shape of the optical cylinder is neglected, except
7 from near-cylinder regions, which were excluded from the field of view (Figure 4). The PIV signal was
8 separated with a 515 nm long-pass filter (CF, Schott OG515) and a 532 ± 4 nm interference filter (IF,
9 ML1 Microcoatings Inc) and detected with a Photron SA1 high-repetition-rate camera. The color glass
10 filter was tilted to approx. 45° to minimize reflections on the cameras on the opposite side of the engine.
11 The phosphorescence signal was collected by two intensified CDD cameras (PIMAX2, Princeton
12 instrument, 16 bit, 1024×1024 pixel, $10 \mu\text{s}$ detection) from the opposite side, separated by a dichroic
13 beamsplitter (Chroma Technology, T410lppt) with a cut-on wavelength of 410 nm and two bandpass
14 filters (BP, Semrock FF01-665/SP) with a FWHM of 266 nm centered at 507 nm (507 ± 133 nm). The
15 cameras were equipped with $f = 50$ mm $f/1.2$ Nikon lenses and are hardware-binned (2×2 pixel). The
16 resulting spatial resolution of the temperature imaging setup is $280 \mu\text{m}$ as measured with a 1951 USAF
17 resolution target. The entire detection system for phosphor thermometry, mounted on a separate optical
18 table, was height-adjustable to optimize the field of view and minimize vignetting effects at higher crank
19 angles, when the field-of-view was partially blocked by the piston. The measurements were carried out
20 with the detector systems set to two heights: An elevated camera position is optimized for 300–420 CAD
21 and a low position for all other measurements.

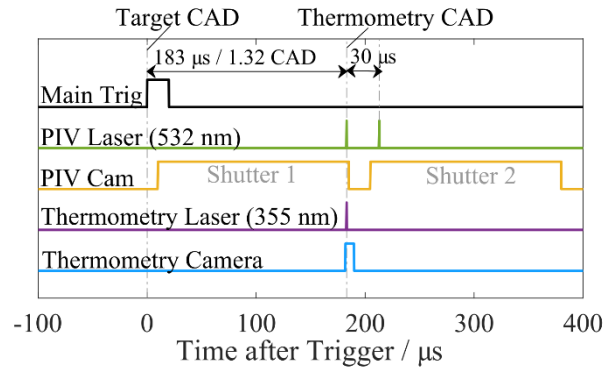


Figure 6: Timing diagram for simultaneous temperature and velocity measurements in an engine.

Error! Reference source not found. shows the timing diagram for simultaneous temperature and velocity measurements in the engine. The main signal was triggered by the crank angle encoder from the engine at the desired crank angle (Target CAD). Cameras and lasers were triggered based on this signal to account for slight deviations from the nominal engine speed. The measurements were performed at 1200 RPM nominal engine speed between 180 and 520 CAD at 20 CAD increments from 180–300 CAD and 400–520 CAD, as well as 330 and 390 CAD. The following measurement sequence was applied for data acquisition: (i) Background images are taken over 200 consecutive engine cycles for each camera and each CAD individually to account for signal contribution from scattered laser light in the absence of phosphor particles. (ii) Particle seeding is activated and the engine is operated for a few cycles until the seeding system operates steadily. Mie scattering images are used to monitor the homogeneity of the particle distribution. (iii) Once the seeding is stabilized, PIV and thermometry data are acquired over 200 consecutive engine cycles at the target CAD.

Measurements were carried out alternately in the compression and expansion stroke to minimize systematic errors. Preceding every measurement day, a compression test of the optical engine was performed to ensure repeatability of the measurements. The piston rings and the optical cylinder were replaced if the compression ratio was significantly impacted by wear or if the transparency of the cylinder was limited through scratches. In general, seeded engine operation was reduced to a minimum to limit wear of the optical cylinder and thus change in background signal. After three measurement sequences, the cylinder head was dismantled for cleaning. Compression tests were performed before and after cleaning to ensure repeatability. The pressure traces from 500 consecutive cycles in motored operation are shown in Figure 7. The variation of the mean pressure traces from each run are within the cycle-to-cycle variations of the other.

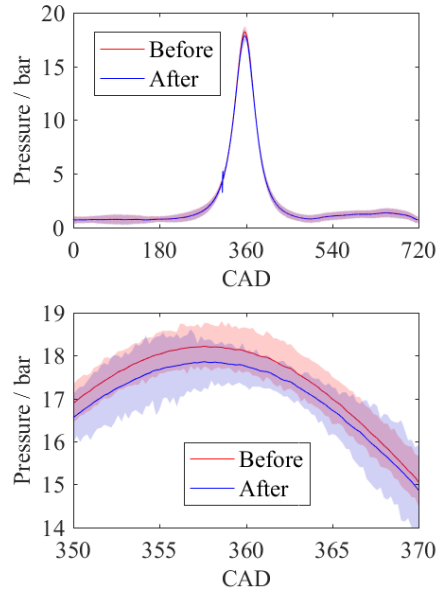


Figure 7: Pressure trace before and after dismounting and cleaning the optical engine under motored operation. Bottom: enlargement around TDC. Transparent overlay: variation in pressure from 500 consecutive cycles. The mean pressure traces are shown with a solid line.

3.5 Data processing

Two-color luminescence and Mie scattering (PIV) raw images are mapped to a global reference coordinate system using a transformation matrix generated in DaVis 8.0 (LaVision GmbH), based on a double-sided calibration plate (LaVision 106–10). The PIV images are then processed using a multi-pass cross-correlation algorithm with iteratively decreasing the interrogation window size from 64×64 to 16×16 pixels with 50 % overlap, leading to a final vector resolution of 1.6 mm^2 .

The raw images from the two luminescence cameras were corrected for non-uniform light collection and signal background. Background images recorded for each CAD were subtracted. A dynamic cut-off filter was applied to the resulting images with an upper and lower threshold of 90 and 10 % of the dynamic range of the camera to avoid non-linearities close to the saturation limit of the detector and to discriminate against areas where the signal is governed by background, e.g., by scattered and reflected luminescence. Subsequently, the images from both cameras were spatially averaged by a 5×5 pixel median filter to reduce noise. The signal ratio map is calculated on a pixel-by-pixel basis. Sub-pixel misalignment between both cameras is considered negligible as the spatial resolution of the cameras is not high enough to resolve individual particles ($\sim 0.2 \text{ mm/px}$). Due to pixel binning and spatial averaging, a quasi-continuous temperature map is was achieved.

1 A flatfield correction accounts for non-uniform light collection in the optical system, an effect that is
2 dominated by the spectral angle-dependence of the dichroic mirror used as beam splitter between both
3 cameras. Spatially varying laser fluence over the height of the laser light sheet does not influence the
4 temperature calculation in a ratio-based method as no significant cross-dependence of the laser fluence on
5 the phosphor emission in the signal response of this phosphor was found in the fluence regime of the
6 measurements (section 4.1.2). Performing a reliable flatfield correction in an engine is difficult because
7 the optical system changes at each CAD due to varying positions of moving parts (piston, valves).
8 Therefore, in our measurements, the flatfield correction was achieved by dividing the ratio image from the
9 condition of interest by the ratio image measured at bottom dead center (180 CAD), where the in-cylinder
10 temperature distribution is expected to be close to uniform. Using the temperature at 180 CAD from a
11 zero-dimensional (0D) simulation (section 3.6), the calculated signal-ratio calibration curve from the
12 spectral calibration measurements can be applied to derive the temperature from the two-color signal ratio
13 at each location in the image.

14 **3.6 Temperature determination from 0D simulations**

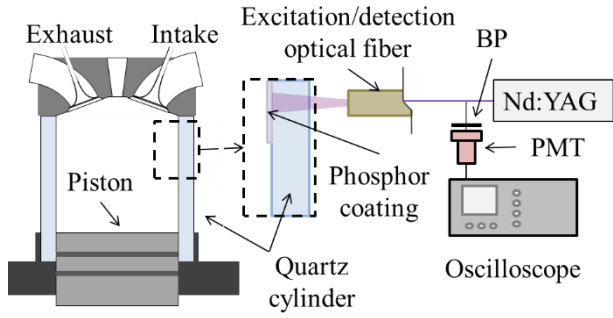
15 A 0D simulation is carried out to estimate the in-cylinder temperature from the reference condition during
16 the compression and expansion stroke and to verify measured temperatures from phosphor thermometry.
17 This is based on the IFPEN engine library developed in the simulation software AMESim® environment
18 [42,43]. In motored operation, the bulk-gas temperature distribution is expected to be homogeneous
19 except for near-wall regions, where heat transfer is not negligible. Under these conditions, the change of
20 the in-cylinder bulk temperature can be calculated with good accuracy following the ideal gas law and
21 wall heat transfer using the heat transfer coefficients introduced by Woschni [44]. The engine geometry is
22 taken into account as well as valve lift and timing. Boundary conditions for intake and exhaust pressure
23 and temperature are acquired during the optical measurements using thermocouples and a piezoelectric
24 pressure sensor (AVL QC34D) resolving the measured value respectively every 1/10 CAD (72 kHz at
25 1,200 RPM). The measurements are averaged over all 200 engine cycles. Heat transfer coefficients from
26 the Woschni model are adjusted in order to match the measured pressure trace.

27 **3.7 Cylinder surface temperature measurements**

28 The calculation of the heat transfer from the in-cylinder gases towards the cylinder requires knowledge of
29 the temperature of the inner surface of the quartz cylinder. The wall temperature was measured with
30 phosphor thermometry using a thin layer of ZnO:Zn (HPC Binder, ZYP Coatings Inc.). An optical fiber is
31 used for illumination (355 nm) and signal collection for detection with a photomultiplier (PMT) equipped
32 with a band pass filter (BP, 505 ± 10 nm) according to Figure 8. There are no focusing optics attached to
33 the fiber as it was very close to the optical cylinder (approx. 20 mm). The measurements are performed for

1 various CAD, averaging 500 engine cycles under motored operation and temperatures are determined
2 from the temporal signal lifetime according to [20]. The results reveal that the in-cylinder wall
3 temperature is approximately constant 357 K ($\sigma = 5$ K) during motored operation.

4



5

6 Figure 8: Setup for measurement of the in-cylinder wall temperature in the motored engine via phosphor thermometry
7 using the luminescence lifetime approach.

8 4 Results and discussion

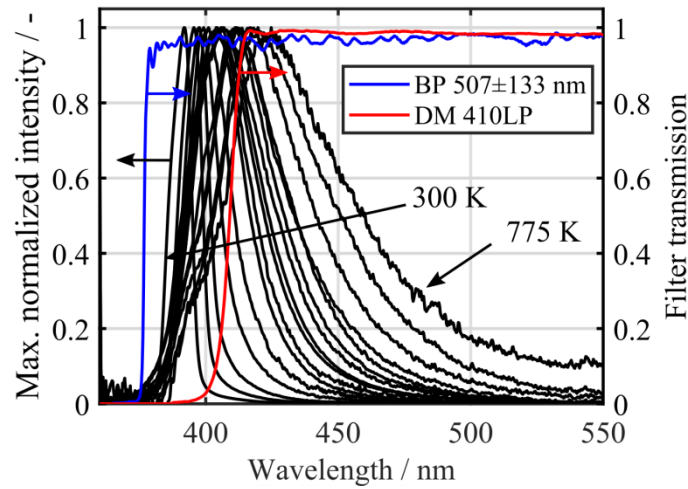
9 4.1 Spectral aerosol characterization

10 For interpretation and calibration of the two-color phosphor thermometry measurements in the engine, the
11 spectral properties of aerosolized ZnO:Zn must be known. Previous work showed that spectral data from
12 powder measurements cannot be transferred to aerosol measurements without causing major bias. It was
13 also observed that the seeding density (particle number density, PND) influences the spectral response
14 [27]. Variations in PND are not only inherently present in a reciprocal engine for measurements in various
15 CAD, as the volume of the particle-laden air changes during the compression and expansion process, but
16 are also subject to cycle-to-cycle variations in flow at the intake manifold and in the particle seeding
17 system. Fluctuations in laser fluence also occur in practical diagnostics system, leading to potential errors
18 due to non-linear signal response [14]. This requires the investigation of the effect to these parameters
19 (PND, laser fluence) on the emission spectrum of ZnO:Zn.

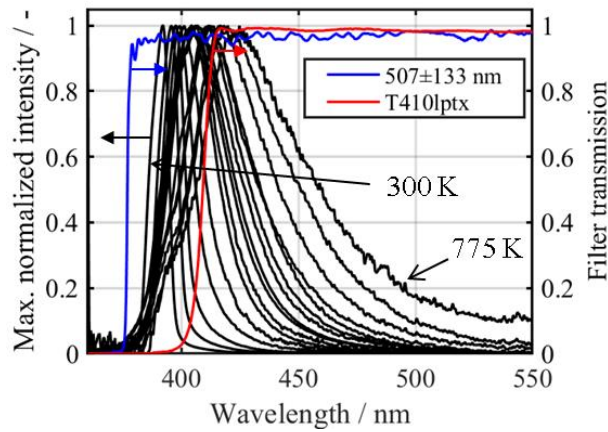
20 4.1.1 Temperature dependence

21 Figure 9 shows normalized phosphor emission spectra for a temperature range between 300 and 775 K,
22 expressing a pronounced shift towards longer wavelengths as temperature increases. This feature is
23 exploited for temperature measurements. To measure temperature in the environment of interest, the ratio
24 between phosphor luminescence from two different emission bands, defined by the optical filter set, is

1 calculated. Therefore, a temperature-ratio calibration is required for each combination of filters. The
 2 intensity for each channel is obtained by convoluting the spectrum with the filter transmission profiles.



3

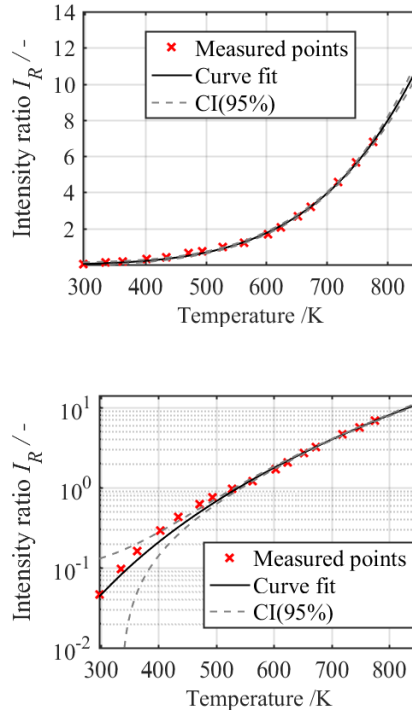


4

5 Figure 9: Normalized phosphor emission intensity for aerosolized ZnO:Zn phosphor at 50 mJ/cm² for temperatures between 300
 6 and 775 K (30 K increments). Transmission characteristics of the filters and mirrors are shown in color.

7 A dichroic beam splitter with 410 nm cut-on wavelength (Chroma Technology, T410lptx) and two
 8 bandpass filters (507 ± 133 nm, Semrock FF01-665/SP) were used for temperature measurements in the
 9 engine and thus the calibration curve was calculated using the transmission profile of these filters. The
 10 laser excitation fluence is 50 mJ/cm², similar to engine measurements. A dichroic beam splitter was used
 11 to increase the signal yield compared to a 50/50 beam splitter. This is particularly important as the global
 12 emission intensity at increased temperatures is low due to thermal quenching. However, due to the angle-
 13 dependence of the dichroic coating, it is suggested for further measurements to separate the spectral
 14 bandpass region from the filters from the cut-on wavelength of the dichroic mirrors for future
 15 measurements.

1 Figure 10 shows the calibration curve which is used in the engine experiments to convert measured ratio
 2 to temperature. The logarithmic plot (bottom) helps to visualize the increased uncertainty for the ratio
 3 estimation at lower temperatures, which directly results from the filter choice. The uncertainties from the
 4 fit are also shown in Figure 16. The combination of filters is chosen to favor the high-temperature regime,
 5 which is of interest in the engine conditions.



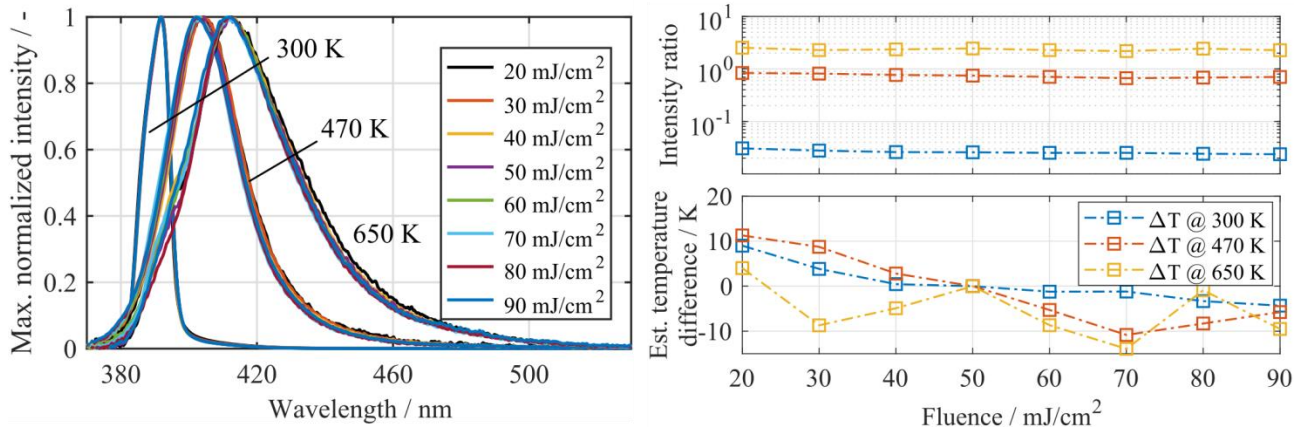
6
 7
 8 Figure 10: Signal ratio-based temperature calibration for ZnO:Zn with a quadratic fit of the experimental data. The dashed lines
 9 show the 95% confidence interval of the fitted calibration curve. The logarithmic plot (bottom) helps to visualize the limited
 10 confidence of the fit for low temperatures.

11
 12 **4.1.2 Laser-fluence dependence**

13 The signal dependence on the laser fluence was investigated in the 20–90 mJ/cm² range at 300, 470, and
 14 650 K (Figure 11). The contribution of readout noise is reduced by recording 200 hardware-accumulated
 15 spectra for each condition. The intensity peak at 355 nm on the spectrometer from elastically scattered
 16 laser light is used as a measure of the seeding density and to account for seeding densities variations
 17 throughout a measurement series. The global emission intensity of each hardware-accumulated spectra is
 18 corrected by the luminescence-equivalent of the seeding density, assuming that the scattering intensity
 19 increases linearly with the seeding density. The data shown are not filtered or smoothed and the spectra
 20 are intensity-normalized for each temperature. The relative standard deviation between spectra for
 21 different laser energies based on the normalized integrated emission between 370 and 500 nm, is $\sigma =$

1 0.6 % for 300 K. This shows that there is negligible influence of the laser fluence on the spectral shape of
 2 phosphorescence emission of ZnO:Zn for near-ambient temperatures in the fluence range applied here.

3



4

5 Figure 11: Left: Emission intensities at 300, 470, and 650 K at varying laser fluences for aerosolized ZnO:Zn. Emission intensities
 6 are normalized to the maximum intensity. Right: Dependence of the signal intensity ratio (top) and the temperature (bottom) to
 7 laser fluence. The lines between data points are visualized to guide the reader's eye. The temperature deviation is estimated
 8 relatively to the fluence of 50 mJ/cm². The filter combination used for measurements in the engine is used to calculate the ratio
 9 and temperature is estimated from the aerosol calibration curve (Figure 10).

10 For increased temperatures (470 and 650 K), the spectra show a slight deviation of $\sigma = 1.7$ and 2.1 %,
 11 respectively. A slight systematic blue-shift of the spectra is observed at 470 K for increasing fluences,
 12 where the peak position shifts from 405 to 402 nm. Given the fact that ZnO:Zn emission spectra shift
 13 towards the red at increasing temperature, this effect cannot be attributed to laser-induced particle heating.

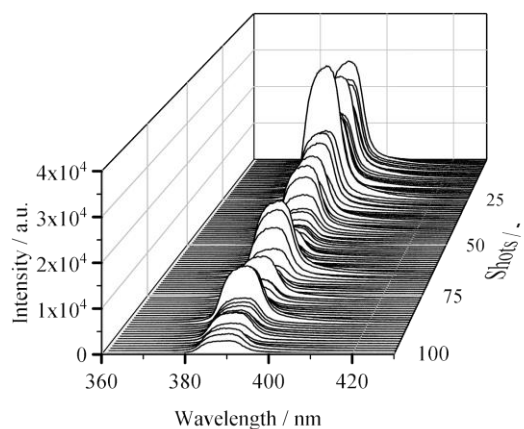
14 Figure 11 (top right) shows the signal intensity ratio from the emission spectra for various laser fluences at
 15 three different temperatures. The ratios are calculated by convoluting the filter transmission curves, which
 16 were used for the measurements in the engine and converted to temperature with the aerosol ratio-
 17 temperature calibration curve (Figure 10). The bottom figure shows the temperature deviation for varying
 18 laser fluences. The temperature deviation is normalized towards the temperature at 50 mJ/cm², which is
 19 the fluence used in engine measurements. The estimated temperature shows a maximum error of 13 K
 20 (4.4 %), 22 K (4.7 %) and 18 K (2.7 %) at 300, 470, and 650 K, respectively. This error is considered
 21 negligible for temperature determination, especially as the calibration and measurements in the engine are
 22 performed at the same fluence.

23 4.1.3 Influence of the seeding density

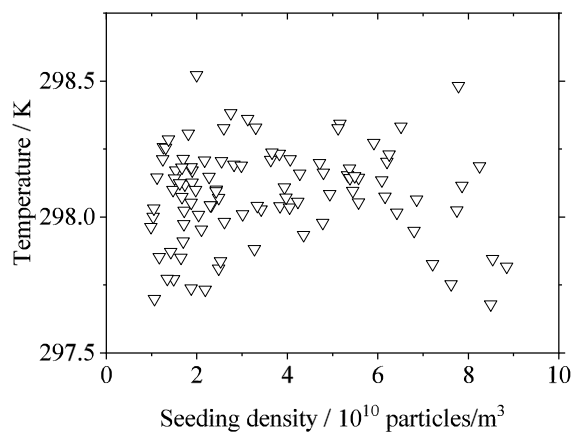
24 In the literature, spectral broadening is reported for increasing seeding density (particle number density,
 25 PND) for aerosolized BAM:Eu [27]. The origin of this behavior is inconclusive, but this implies that

1 varying PND can lead to a potential bias in temperature calculation. Therefore, the influence of the PND
2 on the spectral properties of ZnO:Zn is studied in the aerosol characterization setup (Figure 3). The
3 procedure of particle detection and counting is similar to that in Ref. [35]. The collection apparatus
4 provided a field of view of $40 \times 30 \text{ mm}^2$ with a $16\text{-}\mu\text{m}$ pixel size. The resolution is sufficient to resolve
5 PNDs in the order of $10^{10}\text{--}10^{11} \text{ particles/m}^3$, neglecting out-of-plane signal contribution from indirect
6 illumination. Given the fact that a particle, including its flare effects, is projected on four pixels on the
7 particle counting camera, the maximum measurable PND is $1.4 \times 10^{11} \text{ particles/m}^3$, under the prerequisite
8 that two particles need to be separated by at least one pixel in the camera to be detected as two distinctive
9 particles.

10



11



12

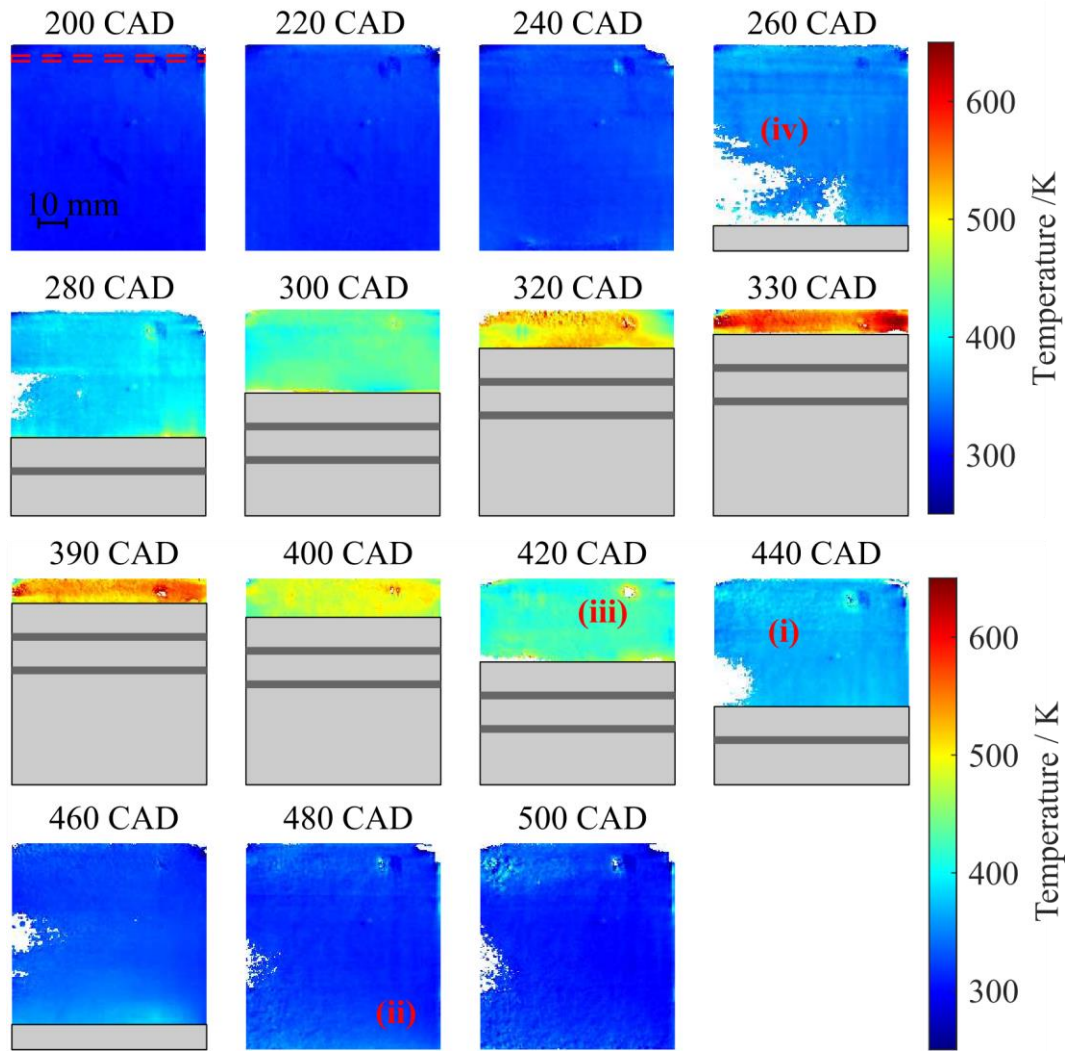
1 Figure 12: 100 single shot emission spectra (top) and estimated temperature (bottom) as a function of the seeding density for
2 aerosolized ZnO:Zn particles at 20 mJ/cm² at ambient temperature (298 K). The filter combination and calibration curve used for
3 temperature estimation are presented in section 4.1.1.

4 This study is performed at ambient temperatures and the laser fluence is set to 20 mJ/cm² with negligible
5 shot-to-shot fluctuations (± 0.2 mJ/cm²). The PND is changed by varying the nitrogen mass flow through
6 the seeder at constant magnetic agitation. The PND, measurement obtained from the particle counting
7 system, and the acquired emission spectra are studied to assess the influence of PND on the temperature
8 calculation. Figure 12 (top) shows 100 emission spectra from ZnO:Zn at 298 K, where the variation of
9 absolute intensities observed in the raw spectra is related to varying PND. By convoluting the filter
10 transmission curves, used in the engine measurements, with the collected spectra, the luminescence of
11 each channel is calculated to obtain the ratio between both luminescence channels. The calibration curve
12 from aerosol measurements is used to transpose the ratio to temperature. Figure 12 (bottom) shows the
13 calculated temperature as a function of the PND. This study shows that the influence of the seeding
14 density on temperature calculation is negligible for the investigated range of PND.

15 **4.2 Measurements in the optical engine**

16 **4.2.1 Temperature measurements**

17 In-cylinder temperature measurements for motored engine operation are presented in Figure 13 for 200 to
18 500 CAD. The images are corrected and post-processed according to the procedure described in section
19 3.5. The temperature fields are calculated from 200 averaged images and show a uniform in-cylinder
20 temperature distribution. However, some systematic non-uniformities are observed and are considered as
21 artifacts of the measurement. Horizontal lines, highlighted with red (i), are visible at some crank angles
22 which are marks on the optical cylinder from the piston rings when the piston is located at TDC. Vertical
23 lines (ii) are likely to stem from progressing cylinder wear throughout the measurements. Other features
24 include some areas, where the background correction was not sufficient to eliminate scattered laser light
25 (iii) due to increasing cylinder wear or particle sticking to the cylinder. White areas on the temperature
26 maps (iv) represent zones, where a local particle number density, thus low signal level, or excessive pixel
27 intensity prevents temperature calculations (see section 3.5). This becomes even more predominant in the
28 single shot images as shown at the end of this section (Figure 15).

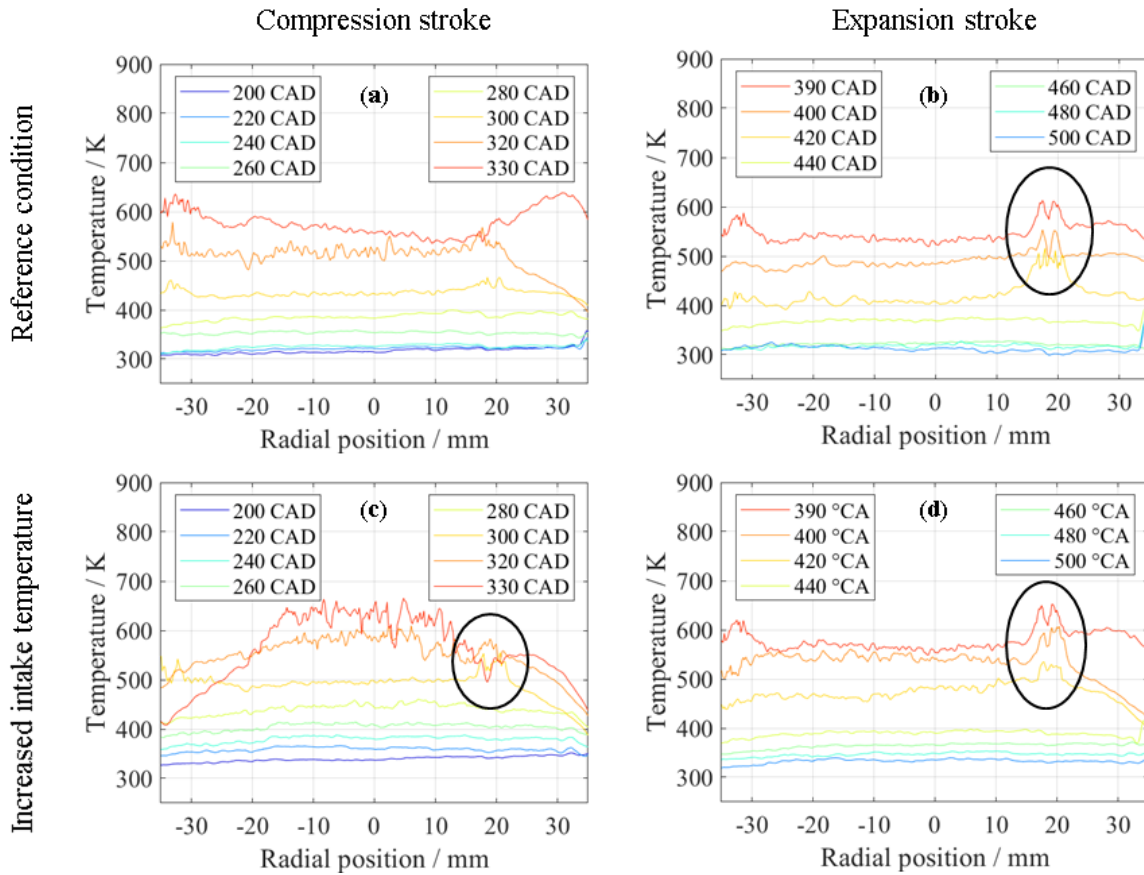


1
 2 Figure 13: Ensemble-averaged maps of the in-cylinder temperature distribution in motored operation in the reference condition
 3 for various crank angles. Systematic non-uniformities are pointed out as i–iv. The red box at 200 CAD highlights the region used
 4 to extract temperature profiles (10 pixel rows).

5 A horizontal temperature profile is extracted from ten pixel rows close to the cylinder head (annotated
 6 with a surrounding red box in the temperature map at 200 CAD in Figure 13). As expected, the in-cylinder
 7 temperature increases during compression and decreases during expansion stroke. For some conditions, a
 8 blank spot (shown in white) is visible due to insufficient signal (i.e., particles) in the respective regions.

9 Figure 14 shows spatial temperature profiles for several CAD during the compression and expansion
 10 stroke at standard conditions ($T_{\text{intake}} = 298$ K, Figure 14 a–b) and increased intake temperature
 11 ($T_{\text{intake}} = 333$ K, Figure 14 c–d). Note that temperature images from different measurement conditions
 12 (reference condition, increased tumble or increased intake temperature condition) are corrected by the
 13 same flatfield, which was taken at bottom dead center of the reference condition. This shows the

1 robustness of this measurement approach and enables comparisons of measurements obtained under
 2 varying conditions.



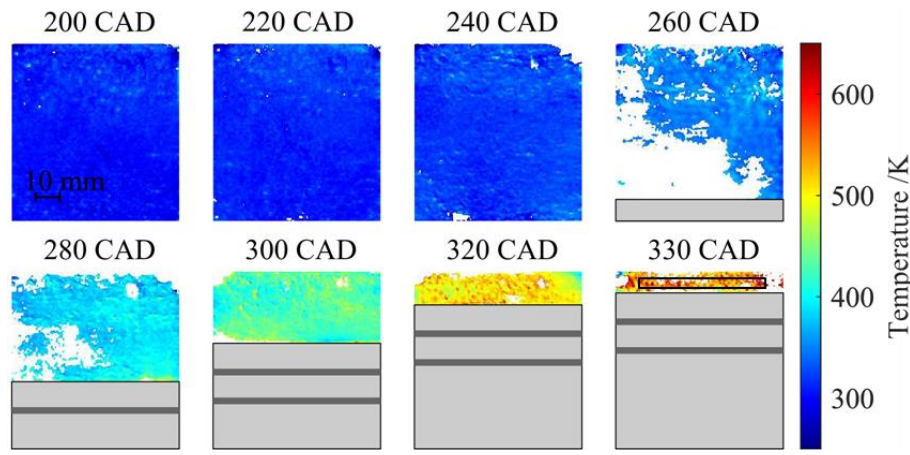
3
 4 Figure 14: Averaged temperature profile across the cylinder for reference condition ($T_{\text{intake}} = 298$ K, a–b) and increased intake
 5 temperature ($T_{\text{intake}} = 333$ K, c–d) for compression (left) and expansion stroke (right). The region highlighted with a black ellipse
 6 is considered an artifact, which are also annotated in the average temperature maps in Figure 13 as region (iii).

7 The increased intake temperature leads to higher in-cylinder temperatures during the entire compression
 8 and expansion stroke, relatively to the reference condition. While the temperature profiles are flat in the
 9 early compression and in the late expansion stroke, a gradient is progressively appearing when
 10 approaching TDC, starting at 300 CAD. The increasing steep, fluctuating ~ 10 K/mm local gradients in the
 11 center of the cylinder at high temperatures (320–420 CAD) are due to the increasing sensitivity for
 12 temperatures above 400 K but is also influenced by increasing uncertainty at high temperatures, as the
 13 luminescence signal of ZnO:Zn decreases due to thermal quenching. This significantly reduces the signal-
 14 to-background ratio and it induces higher uncertainty. In Figure 14, the horizontal temperature profiles
 15 show lower temperatures towards the cylinder walls in (c) relatively to (a), which could potentially be
 16 attributed to increasing heat transfer on the cylinder wall at increasing temperatures. The local temperature
 17 peaks at $r \approx 20$ mm are artifacts caused by light reflection, which can also be see in the 2D temperature

1 images in Figure 13. However, the position used to extract a temperature profile (red box in Figure 13,
 2 200 CAD) is close to the cylinder head. This position was chosen as it enables a direct comparison
 3 between all measured CAD, but features some unwanted scattering from the top of the pent-roof
 4 combustion chamber, which becomes predominant towards the cylinder walls at the “high” camera
 5 position. Generally, the temperature profiles show systematic structures between the two camera positions
 6 (“low” at 180–280 CAD and 440–520 CAD; “high” at 300–330 CAD and 390–420 CAD). Even if two
 7 different flatfields for both camera positions were acquired (both at 180 CAD), it is possible that other
 8 systematic errors are introduced, e.g., due the higher particle number density. This does not change the
 9 luminescence properties of the phosphor (see section 4.1.3) but may alter the contribution of elastically-
 10 scattered light from particles in the engine, which increases the probability of out-of-plane illumination or
 11 the signal contribution from particles sticking to the walls of the optical cylinder. Also, systematic errors
 12 become more significant at high temperatures as the signal intensity decreases due to thermal quenching
 13 (cf. section 4.2.3).

14 The temperature profiles in the expansion stroke are invariably lower compared to those at the equivalent
 15 CAD in the compression stroke (c vs. b), e.g., 480 vs. 240 CAD, which is due to the non-isentropic nature
 16 of the compression process. Despite systematic errors, this demonstrates the capability of this diagnostics
 17 to capture small changes in temperature in challenging measurement conditions.

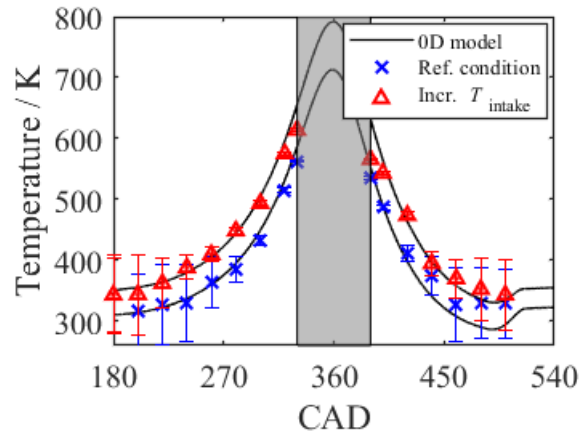
18 Figure 15 shows the single-shot temperature maps from the reference condition between 200–330 CAD.
 19 The white areas were excluded from temperature calculation because the pixel intensity is too low, e.g.,
 20 from low particle number density, or too high from areas, where the background subtraction could not
 21 account for, e.g., elastically scattered laser light.



22
 23 Figure 15: Single-shot temperature field for reference conditions. Note that 180 CAD (bottom dead center) is not shown as it is
 24 used for determining flatfield information, assuming homogeneous temperature. White: Areas excluded from analysis because of
 25 insufficient signal. The area highlighted with a box at 330 CAD is used for single-shot precision calculations.

1 4.2.2 Measurement accuracy and precision

2 Figure 16 shows the temporal temperature trace calculated from the in-cylinder pressure from the 0D
3 simulation together with the gas temperature derived from two-color phosphor thermometry
4 measurements for two operating conditions. The rise in temperature starting at 500 CAD in the 0D model
5 is due to the fact that the exhaust manifold pressure is higher than in-cylinder pressure. Therefore, the
6 cylinder pressure (and thus the temperature calculated in the model) increases as soon as the exhaust valve
7 opens (0.7 mm exhaust valve lift at 500 CAD).



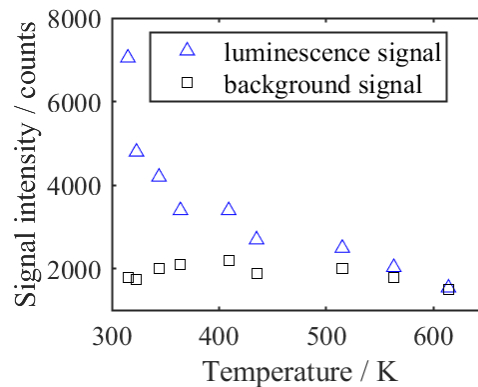
8
9 Figure 16: Simulated in-cylinder temperature calculated from the 0D model (solid black line) and measured temperatures derived
10 from two-color phosphor thermometry. The error bars show the estimated calibration error as discussed in sections 4.2.3 and
11 4.1.1.

12 The temperatures measured with phosphor thermometry show good agreement with the simulation. The
13 error bars for the temperatures from optical measurements visualize an estimated error from the filter
14 combination used in this work for calibration and measurements (section 4.1.1). For 300–420 CAD, the
15 thermographic measurements are systematically lower than the simulated values, which might be related
16 to systematic errors or to the application of the flatfield. The upper and the lower limit of the confidence
17 interval (95 %) is used to estimate the accuracy of this technique. The measurement uncertainty at 300 K
18 is found to be 55 K (18 %) and 2 K (0.3 %) at 614 K due to errors in the calibration. It is clear that the
19 current filter combination chosen for engine measurements favors elevated temperatures.

20 The measurement precision is derived from 200 single shot images ($\pm 1\sigma$ basis) around the mean value
21 from a constant ROI ($62 \times 5 \text{ mm}^2$) throughout all crank angle degrees where the temperature was close to
22 uniform. The ROI used for precision calculation is highlighted in Figure 15. The measurement precision
23 for the reference condition decreases from 3.7 K at 317 K (1.2 %) to 17.3 K at 515 K (3.3 %) at 200 and
24 320 CAD respectively. For the increased intake temperature case, the uncertainty increases from 2.3 K
25 (0.6 % at 343 K to 24.4 K (4.2 % at 575 K) at 200 and 320 CAD.

1 4.2.3 Uncertainty quantification

2 The accuracy and precision have been discussed in the previous section, however, this technique also
3 suffers from low signal intensities at high temperatures due to thermal quenching, affecting both accuracy
4 and precision. Figure 17 shows the evolution of the measured background and luminescence signal at
5 increasing temperatures. The background consists of spatially and temporally varying sources, including
6 out-of-plane illumination or particles sticking to the piston or cylinder walls. The luminescence camera
7 counts were extracted from an area of $8 \times 8 \text{ mm}^2$, where the signal is approximately uniform. The signal to
8 noise ratio (SNR) decreases from 3.9 at 300 K to 1.033 at 614 K. It is possible that this is responsible for
9 the underestimation in temperature at 330 and 390 CAD for the increased intake temperature condition.
10 Furthermore, the average temperature needs to be interpreted with care in the regions, where temperature
11 calculation is not possible from all cycles, because one or both cameras are below the intensity threshold,
12 as the overall average might be biased towards lower temperatures. This shows the intrinsic problem of
13 increasing uncertainty at high temperatures for measurement using thermographic phosphors due to
14 thermal quenching.



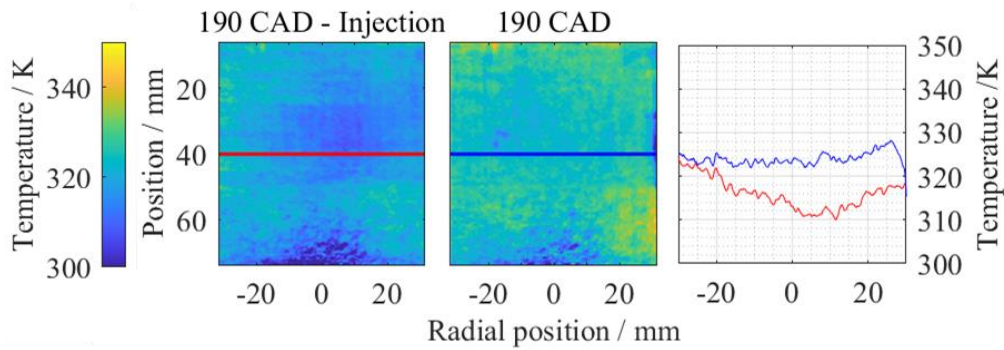
15
16 Figure 17: Luminescence and background signal intensities at increasing in-cylinder temperatures.

17

18 4.2.4 Spray injection

19 Temperature measurements using phosphor thermometry were also carried out after fuel injection at
20 increased intake temperature (330 K). Non-fluorescent fuel (*n*-pentane) is injected at 170 CAD using a
21 five-hole injector (Bosch GDI HDEV 5.2) operated at 200 bar injection pressure. Figure 18 shows the
22 average temperature map at 190 CAD (left) and the temperature profile (right) derived from an average
23 over ten pixels 55 mm below the injector tip after injection. At 190 and 200 CAD (not shown) there is a
24 temperature difference of approximately 15 and 10 K respectively. A comparison with the reference
25 temperature profile from motored operation (no fuel injection) shows that the temperature drop due to

1 evaporative cooling can be visualized. The single shot precision (1σ basis) from the evaluated temperature
 2 profile without injection is 4.7 K (1.5 % at 324 K), so it is clear that the measured temperature difference
 3 is of non-statistical nature. To verify these results, an estimation of the expected temperature was
 4 performed based on adiabatic fuel-air mixing using the one-dimensional spray model developed in [45].
 5 For the conditions of this study, the two temperature gaps of 15 and 10 K, measured at 190 and 200 CAD,
 6 correspond to a fuel mass fraction of $Y_f = 0.34$ and 0.24, respectively. These values are expected at this
 7 stage of mixing and also obtained in similar studies [46].

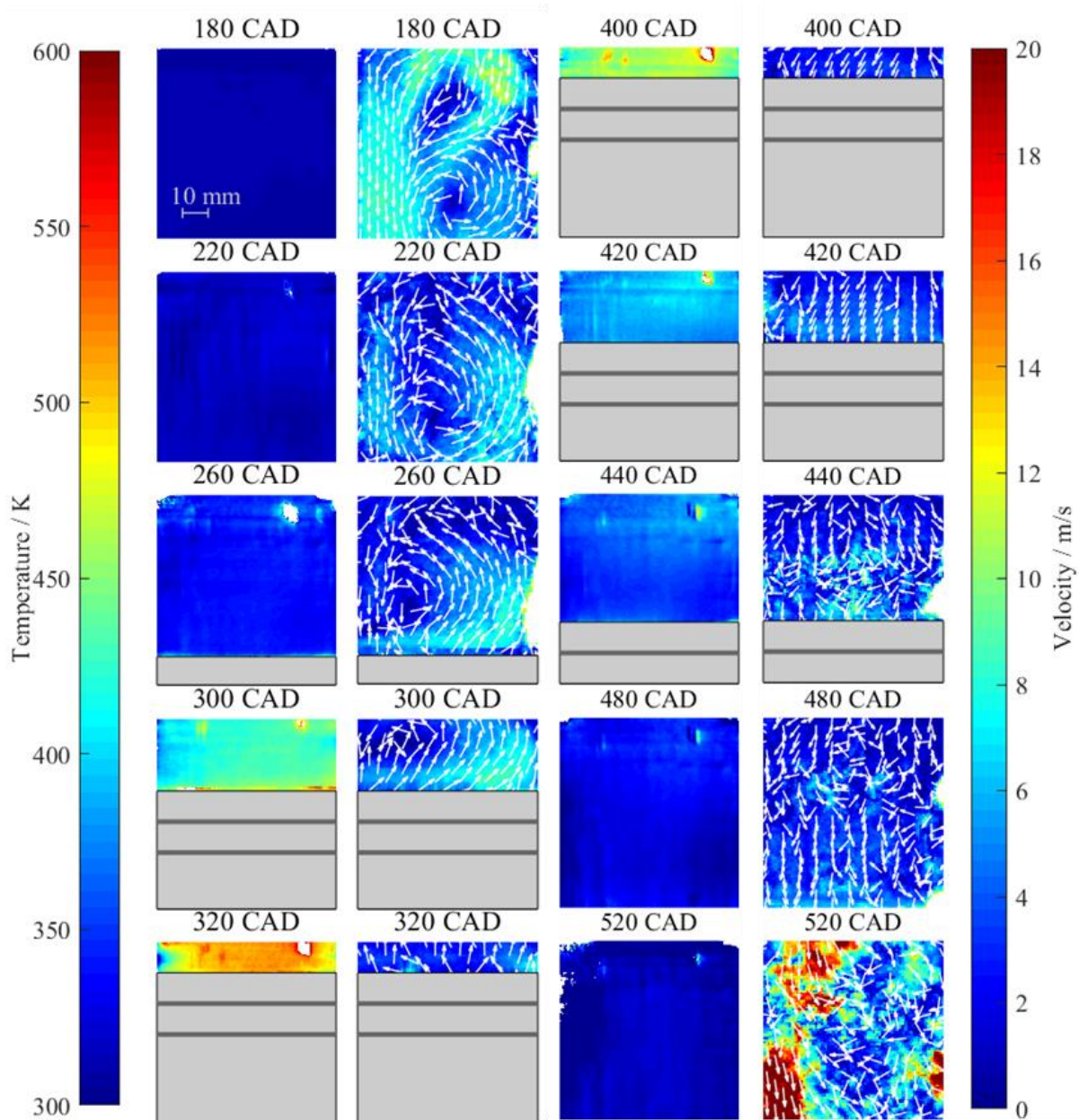


8
 9 Figure 18: Average temperature field (left and center) of the in-cylinder gas and temperature profile (right) with and without fuel
 10 injection. The reference temperature profile from motored operation (no fuel injection) is annotated in blue. The vertical position
 11 is given relatively to the viewing plane shown in Figure 4.

12

13 4.2.5 Simultaneous T-PIV measurements in the engine

14 Results of simultaneous temperature and velocity measurements are shown in Figure 19 for the increased
 15 tumble operating condition. While the temperature measurements have been discussed in section 4.2,
 16 velocity measurements will be emphasized in this section. The velocity field during the compression
 17 stroke shows the emergence of a main vortex centered in the middle of the combustion chamber,
 18 corresponding to the typical tumble flow motion. As these measurements are carried out in motored
 19 operation, the flow field is not affected by fuel injection or evaporation. The center of the tumble flow
 20 moves upwards as the piston approaches TDC and the flow does not collapse until 320 CAD. The flow
 21 field during the expansion stroke is mainly governed by the down movement of the piston as there is no
 22 further turbulence induced by combustion. At 520 CAD the impact of the reverse flow from the exhaust
 23 manifold towards the cylinder can be clearly seen, occurring due to the positive pressure difference between exhaust
 24 manifold and in-cylinder pressure at exhaust valve opening. These results demonstrate that this diagnostics
 25 approach is capable to capture the main aerodynamic features found in a spark-ignition engine [46–48].



1
 2 Figure 19: Simultaneous temperature and velocity fields from the operation condition “increased tumble”. The intake valves are
 3 located on the top right, and the exhaust valve on the top left of the image. The flatfield correction is performed towards bottom
 4 dead center of the reference condition. For improved visibility, only every second velocity vector is shown.

5 Summary and conclusions

6 In this work, simultaneous measurements of in-cylinder temperature and velocity fields were performed
 7 under motored conditions using thermographic phosphor particles as tracer. From spectroscopic
 8 measurements of three commercially available phosphors (BAM:Eu, ZnO, ZnO:Zn), ZnO:Zn was selected
 9 for the engine measurements due to favorable luminescent properties such as high temperature sensitivity,

1 short radiative lifetimes, and the absence of non-linear dependence of the laser fluence on the luminescent
2 emissions. The spectroscopic properties of aerosolized ZnO:Zn were determined up to 775 K. These
3 measurements showed that variations in particle number density and laser fluence have a negligible
4 influence on the spectral properties that are the basis of two-color thermometry.

5 Combined thermometry and velocimetry measurements (T-PIV) were successfully performed in the
6 engine over a wide range of crank angles (180 to 520 CAD) using ZnO:Zn as a thermographic phosphor
7 as tracer particles. At increasing CAD, artifacts are observed at the outer zones close to the walls of the
8 optical cylinder. They are attributed to signal contribution from the cylinder walls and deficiencies of the
9 flatfield correction that is based on the temperature field of the reference condition at bottom dead center
10 for all measurements. The temperatures, derived from two-color detection of the luminescence of ZnO:Zn
11 showed excellent agreement with the in-cylinder bulk gas temperatures from a 0D simulation. Despite the
12 good precision (24.4 K or 4.2 % uncertainty at 575 K in averaged images), for measurements at high
13 temperatures, this technique suffers from low signal intensities at increasing temperature, inherently
14 increasing the measurement uncertainty. This diagnostics method was also successfully applied to
15 visualize evaporative cooling effects of the cylinder charge following a direct-injection event. This
16 technique can be further improved by using phosphors with higher quenching temperatures at short
17 emission decay times to decrease the uncertainty. Additionally, a deeper understanding of phosphor
18 degradation mechanisms is required to enable measurement in the post-combustion regime.

19 **Declaration of Competing Interest**

20 The authors declare that they have no known competing financial interests or personal relationships that
21 could have appeared to influence the work reported in this paper.

22 **Acknowledgements**

23 This research did not receive any specific grant from funding agencies in the public, commercial, or not-
24 for-profit sectors.

25

1 **6 Appendix**

2 **6.1 A1 Tumble calculation**

3 The dimensionless tumble ratio is defined as the quotient between the tangential (v_t) and the vertical gas
4 velocity v_v along the axis perpendicular to the axis of the of the engine cylinder.

$$5 \quad TR = \frac{v_t}{v_v}$$

6 The tumble ratio of a cylinder head is calibrated on a static aerodynamic flow bench. The vertical velocity
7 is calculated from the pressure p_0 in the intake manifold and the pressure difference Δp from the intake
8 manifold and the outlet tube representing the engine cylinder, measured by pressure transducers, where ρ
9 is the density and κ the isentropic exponent of the gas.

$$10 \quad v_v = \sqrt{2 \cdot \frac{\kappa}{\kappa - 1} \cdot \frac{p_0}{\rho_0} \cdot \left[1 - \left(\frac{p_0 - \Delta p}{p_0} \right)^{\frac{\kappa - 1}{\kappa}} \right]}$$

11 The tangential velocity is calculated from angular momentum of a gas flow, where the righting torque M
12 exerted by the flow is measured directly with a honeycomb torquemeter (Entran ELC-16), and the
13 averaged mass flowrate from both ports of the intake manifold Q and the diameter d of the tube
14 representing the engine bore.

$$15 \quad v_t = \frac{4 \cdot M}{Q \cdot d}$$

16 **7 References**

- 17 [1] R. Opat, Y. Ra, M.A. Gonzalez D., R. Krieger, R.D. Reitz, D.E. Foster, R.P. Durrett, R.M. Siewert,
18 Investigation of Mixing and Temperature Effects on HC/CO Emissions for Highly Dilute Low
19 Temperature Combustion in a Light Duty Diesel Engine, SAE Technical Paper 2007-01-0193
20 (2007).
- 21 [2] C.K. Westbrook, Chemical kinetics of hydrocarbon ignition in practical combustion systems, Proc.
22 Combust. Inst. 28 (2000) 1563–1577.
- 23 [3] P. Priyadarshini, A. Sofianopoulos, S. Mamalis, B. Lawler, D. Lopez-Pintor, J.E. Dec, Understanding
24 partial fuel stratification for low temperature gasoline combustion using large eddy simulations,
25 International Journal of Engine Research 22 (2020) 1872-1887.

- 1 [4] F.J. Arnau, J. Martín, P. Piqueras, Á. Auñón, Effect of the exhaust thermal insulation on the engine
2 efficiency and the exhaust temperature under transient conditions, *International Journal of Engine*
3 *Research* 22 (2020) 2869-2883.
- 4 [5] F. Perini, K. Zha, S. Busch, E. Kurtz, R.C. Peterson, A. Warray, R.D. Reitz, Piston geometry effects
5 in a light-duty, swirl-supported diesel engine: Flow structure characterization, *International Journal*
6 *of Engine Research* 19 (2018) 1079–1098.
- 7 [6] C. Schulz, V. Sick, J. Wolfrum, V. Drewes, M. Zahn, R. Maly, Quantitative 2D single-shot imaging
8 of no concentrations and temperatures in a transparent SI engine, *Symposium (International) on*
9 *Combustion* 26 (1996) 2597–2604.
- 10 [7] M. Luong, W. Koban, C. Schulz, Novel strategies for imaging temperature distribution using
11 Toluene LIF, *Journal of Physics: Conference Series* 45 (2006) 133–139.
- 12 [8] S. Peukert, A. Sallom, A. Emelianov, T. Endres, M. Fikri, H. Böhm, H. Jander, A. Eremin, C.
13 Schulz, The influence of hydrogen and methane on the growth of carbon particles during acetylene
14 pyrolysis in a burnt-gas flow reactor, *Proc. Combust. Inst.* 37 (2019) 1125–1132.
- 15 [9] T. Lee, W.G. Bessler, H. Kronmayer, C. Schulz, J.B. Jeffries, Quantitative temperature
16 measurements in high-pressure flames with multiline NO-LIF thermometry, *Appl. Opt.* 44 (2005)
17 6718–6728.
- 18 [10] B. Peterson, E. Baum, B. Böhm, V. Sick, A. Dreizler, High-speed PIV and LIF imaging of
19 temperature stratification in an internal combustion engine, *Proc. Combust. Inst.* 34 (2013) 3653–
20 3660.
- 21 [11] D. Most, A. Leipertz, Simultaneous two-dimensional flow velocity and gas temperature
22 measurements by use of a combined particle image velocimetry and filtered Rayleigh scattering
23 technique, *Appl. Opt.* 40 (2001) 5379–5387.
- 24 [12] C. Abram, B. Fond, F. Beyrau, Temperature measurement techniques for gas and liquid flows using
25 thermographic phosphor tracer particles, *Prog. Energy Combust. Sci.* 64 (2018) 93–156.
- 26 [13] J. Brübach, A. Dreizler, J. Janicka, Gas compositional and pressure effects on thermographic
27 phosphor thermometry, *Meas. Sci. Technol.* 18 (2007) 764.
- 28 [14] B. Fond, C. Abram, F. Beyrau, Characterisation of the luminescence properties of BAM:Eu²⁺
29 particles as a tracer for thermographic particle image velocimetry, *Appl. Phys. B* 121 (2015) 495–
30 509.
- 31 [15] P.A. Rodnyi, I.V. Khodyuk, Optical and luminescence properties of zinc oxide (Review), *Optics and*
32 *Spectroscopy* 111 (2011) 776–785.
- 33 [16] A. Kopf, M. Bardi, E. Kohler, T. Endres, G. Bruneaux, C. Schulz, Survivability of the thermographic
34 phosphors YAG:Pr³⁺ and SMP:Sn²⁺ in a premixed flame, *Meas. Sci. Technol.* 22 (2021) 74001.

- 1 [17] B. Fond, C. Abram, A.L. Heyes, A.M. Kempf, F. Beyrau, Simultaneous temperature, mixture
2 fraction and velocity imaging in turbulent flows using thermographic phosphor tracer particles, *Opt.*
3 *Express* 20 (2012) 22118–22133.
- 4 [18] J.S. Armfield, R.L. Graves, D.L. Beshears, M.R. Cates, T.V. Smith, S.W. Allison, Phosphor
5 Thermometry for Internal Combustion Engines, in: *International Spring Fuels & Lubricants Meeting*
6 *& Exposition*, SAE International, 1997.
- 7 [19] J. Brübach, T. Kissel, A. Dreizler, Phosphor thermometry at an optically accessible internal
8 combustion engine, in: *Lasers, Sources and Related Photonic Devices*, Optical Society of America,
9 2010, LWA5.
- 10 [20] J.T. Kashdan, G. Bruneaux, Laser-Induced Phosphorescence Measurements of Combustion Chamber
11 Surface Temperature on a Single-Cylinder Diesel Engine, SAE Technical Paper 2011-01-2049
12 (2011).
- 13 [21] R. Hasegawa, Sakata I., Yanagihara H., Johansson B., Omrane A., Aldén M., Two-dimensional gas-
14 phase temperature measurements using phosphor thermometry, *Appl. Phys. B* 88 (2007) 291–296.
- 15 [22] R. Hasegawa, I. Sakata, H. Yanagihara, G. Särner, M. Richter, M. Aldén, B. Johansson, Two-
16 Dimensional Temperature Measurements in Engine Combustion Using Phosphor Thermometry, SAE
17 Transactions 116 (2007) 405–411.
- 18 [23] N. Takada, I. Sakata, H. Yanagihara, J. Lindén, M. Richter, M. Aldén, B. Johansson, Two-
19 Dimensional Temperature Measurements in Diesel Piston Bowl Using Phosphor Thermometry, SAE
20 Technical Paper 2009-24-0033 (2009).
- 21 [24] N.J. Neal, J. Jordan, D. Rothamer, Simultaneous measurements of in-cylinder temperature and
22 velocity distribution in a small-bore diesel engine using thermographic phosphors, SAE International
23 *Journal of Engines* 6 (2013) 300–318.
- 24 [25] G. Jovicic, L. Zigan, S. Will, A. Leipertz, Phosphor thermometry in turbulent hot gas flows applying
25 Dy:YAG and Dy:Er:YAG particles, *Meas. Sci. Technol.* 26 (2014) 15204.
- 26 [26] B. Fond, C. Abram, M. Pougin, F. Beyrau, Characterisation of dispersed phosphor particles for
27 quantitative photoluminescence measurements, *Opt. Mater. Express* 89 (2019) 615–622.
- 28 [27] D. Witkowski, D. Rothamer, Investigation of aerosol phosphor thermometry (APT) measurement
29 biases for Eu:BAM, *Appl. Phys. B* 124 (2018) 202.
- 30 [28] E. Hertle, J. Bollmann, S. Aßmann, V. Kalancha, A. Osvet, M. Batentschuk, S. Will, L. Zigan,
31 Characterization of the phosphor (Sr,Ca)SiAlN₃: Eu²⁺ for temperature sensing, *J. Lumin.* 226 (2020)
32 117487.
- 33 [29] D. Witkowski, D. Rothamer, Scattering referenced aerosol phosphor thermometry, *Meas. Sci.*
34 *Technol.* 30 (2019) 44003.

- 1 [30] B. Fond, C. Abram, M. Pougin, F. Beyrau, Investigation of the tin-doped phosphor
2 $(\text{Sr,Mg})_3(\text{PO}_4)_2:\text{Sn}^{2+}$ for fluid temperature measurements, *Opt. Mater. Express* 9 (2019) 802–818.
- 3 [31] Y. Zhang, B. Lin, X. Sun, Z. Fu, Temperature-dependent photoluminescence of nanocrystalline ZnO
4 thin films grown on Si (100) substrates by the solgel process, *Appl. Phys. Lett.* 86 (2005) 131910.
- 5 [32] G. Särner, M. Richter, M. Aldén, Investigations of blue emitting phosphors for thermometry, *Meas.*
6 *Sci. Technol.* 19 (2008) 125304.
- 7 [33] B. Li, J. Lindén, Z.S. Li, A.A. Konnov, M. Aldén, L.P.H.d. Goey, Accurate measurements of laminar
8 burning velocity using the Heat Flux method and thermographic phosphor technique, *Proc. Combust.*
9 *Inst.* 33 (2011) 939–946.
- 10 [34] G. Särner, M. Richter, M. Aldén, Two-dimensional thermometry using temperature-induced line
11 shifts of ZnO:Zn and ZnO:Ga fluorescence, *Opt. Lett.* 33 (2008) 1327–1329.
- 12 [35] Fond, Benoît and Abram, Christopher and Beyrau, Frank, On the characterisation of tracer particles
13 for thermographic particle image velocimetry, *Applied Physics B* 118 (2015) 393–399.
- 14 [36] C. Abram, B. Fond, F. Beyrau, High-precision flow temperature imaging using ZnO thermographic
15 phosphor tracer particles, *Opt. Express* 23 (2015) 19453–19468.
- 16 [37] van Lipzig, J. P. J., M. Yu, N.J. Dam, C.C.M. Luijten, de Goey, L. P. H., Gas-phase thermometry in
17 a high-pressure cell using BaMgAl10O17:Eu as a thermographic phosphor, *Applied Physics B* 111
18 (2013) 469–481.
- 19 [38] Satoshi Someya, Yasuhiro Okura, Mitsunori Uchida, Yoshihisa Sato, Koji Okamoto, Combined
20 velocity and temperature imaging of gas flow in an engine cylinder, *Opt. Lett.* 37 (2012) 4964–4966.
- 21 [39] J. Lindén, N. Takada, B. Johansson, M. Richter, M. Aldén, Investigation of potential laser-induced
22 heating effects when using thermographic phosphors for gas-phase thermometry, *Applied Physics B*
23 96 (2009) 237–240.
- 24 [40] F.W. Bowditch, A New Tool for Combustion Research A Quartz Piston Engine, SAE Technical
25 Paper 610002 (1961).
- 26 [41] D. Maligne, J. Kashdan, V. Ricordeau, Base de données ide: moteur optique: Projet ICAMDAC:
27 Phase 4.1. IFPen.
- 28 [42] S. Richard, S. Bougrine, G. Font, F.-A. Lafossas, F. Le Berr, On the Reduction of a 3D CFD
29 Combustion Model to Build a Physical 0D Model for Simulating Heat Release, Knock and Pollutants
30 in SI Engines, *Oil & Gas Science and Technology - Rev. IFP* 64 (2009) 223–242.
- 31 [43] F.-A. Lafossas, O. Colin, F. Le Berr, P. Menegazzi, Application of a new 1D combustion model to
32 gasoline transient engine operation, SAE Technical Paper 2005-01-2107 (2005).
- 33 [44] G. Woschni, A Universally Applicable Equation for the Instantaneous Heat Transfer Coefficient in
34 the Internal Combustion Engine, SAE Technical Paper 670931 (1967).

1 [45] J.V. Pastor, J. J.M. García, J.M. Pastor, A 1D model for the description of mixing-controlled inert
2 diesel sprays, *Fuel* 87 (2008) 2871–2885.

3 [46] M. Ritter, L.-M. Malbec, O. Laget, Assessment and Validation of Internal Aerodynamics and
4 Mixture Preparation in Spark-Ignition Engine Using LES Approach, SAE Technical Paper 2020-01-
5 2009 (2020).

6 [47] R.B.R. Da Costa, R.M. Braga, C.A. Gomes Júnior, R.M. Valle, R. Huebner, PIV measurements and
7 numerical analysis of in-cylinder tumble flow in a motored engine, *Journal of the Brazilian Society
8 of Mechanical Sciences and Engineering* 39 (2017) 3931–3945.

9 [48] I. Ko, F. Rulli, S. Fontanesi, A. d’Adamo, K. Min, Methodology for the large-eddy simulation and
10 particle image velocimetry analysis of large-scale flow structures on TCC-III engine under motored
11 condition, *International Journal of Engine Research* 22 (2020) 1-23.

12
13
14